

Radar-based interactive multi-model multi-target tracking algorithm for UAV swarms

Jianwei Ren¹, Hua Wang², Hao Rong², Zexian Wei^{2,*}, Peixia Lv², Xiuqiong Li², and Mou Bai²

¹ Guangxi Beibu Gulf Investment Group Co., Ltd, Nanning, 530029, PR China

² Guangxi Transportation Science and Technology Group Co., Ltd, Nanning, 530007, PR China

Received: 25 December 2025 / Accepted: 13 February 2026

Abstract. With the gradual opening of low-altitude airspace and the rapid development of UAV technology, large-scale UAV swarms are increasingly used in logistics, inspection, and security scenarios. To achieve accurate and robust tracking of highly dynamic, high-density, and strongly interactive UAV swarms, this study proposes a radar-based interactive multi-model multi-target tracking algorithm. Point cloud quality is improved by integrating velocity vector density clustering with adaptive constant false alarm rate detection. An interactive multi-model framework incorporating uniform velocity, uniform acceleration, and coordinated turning modes is established, together with a group potential field-driven state transition mechanism. Adaptive thresholding and dynamic track splitting and merging strategies are further introduced to enhance tracking stability. Experimental results show that the proposed method achieves an average distance RMSE of 1.47 m and a speed RMSE of 1.18 m/s, representing reductions of 49.8% and 42.3% compared with the traditional joint probability data association algorithm. The average tracking accuracy reaches 88.19% and remains 84.31% under a clutter density of 80 points/scan, while the average computation time is 36.92 ms, satisfying real-time requirements. The results demonstrate improved accuracy and stability for low-altitude UAV surveillance in high-density urban scenarios.

Keywords: UAV swarm / multi-target tracking / interactive multi-model / radar signal

1 Introduction

With the gradual opening of low-altitude airspace and the rapid development of Unmanned Aerial Vehicle (UAV) technology, large-scale UAV clusters are increasingly used in logistics, inspections, security, and other scenarios, and the resulting aerial supervision and safety challenges have become increasingly prominent [1]. As an all-weather, all-weather active detection method, radar has unique advantages against non-cooperative UAV targets under complex meteorological and lighting conditions. However, when faced with UAV groups with high density, strong interaction, and changing maneuver modes, the performance of traditional Multi-Target Tracking (MTT) algorithms often drops sharply due to ambiguous data association, insufficient model adaptability, and failure to effectively model group dynamic coupling. Therefore, there is an urgent need to develop an advanced tracking method that can deeply integrate radar sensing characteristics and group behavior rules to support the reliable operation of future low-altitude intelligent transportation systems [2,3].

In recent years, the academic community has carried out many explorations around the problem of multi-UAV tracking. Zhang B et al. proposed a joint probabilistic data correlation filtering framework, which effectively suppresses false measurement interference in low-density scenarios. However, this method was prone to track exchange when targets intersect, mainly because when the two target trajectories were highly close, the sparsity assumption of the correlation probability matrix was broken, leading to correlation decision bias [4]. Moon J et al. introduced an interactive multi-model structure and dynamically switched between uniform speed, turning and acceleration models through the Markov transfer mechanism. Its innovation lied in the use of model probability weights to adapt to changes in target maneuvering modes in real-time. However, this method did not consider the interaction between targets, such as the cooperative obstacle avoidance behavior of adjacent individuals when a UAV group flies in formation. This type of group dynamic characteristics could not be characterized by a single-target kinematic model [5]. Zhou W H et al. used stochastic finite set theory to construct a probability hypothesis density filter, avoiding the traditional data association process by directly estimating the target distribution function.

* Corresponding author: zexian999@outlook.com

However, when the target distance was smaller than the radar beamwidth, the ambiguity of the point cloud data would lead to distortion of the probability density function estimation [6].

With the rapid advancement of deep learning in computer vision, deep neural network-based visual tracking methods have emerged as a research hotspot. By learning end-to-end feature representations, deep learning models significantly enhance tracking robustness and accuracy. For instance, convolutional neural networks extract deep semantic features combined with temporal correlation modules to address challenges such as appearance variations and background interference. Muslimov T Z et al. used deep learning for measurement generation and state prediction, and improved nonlinear modeling capabilities through end-to-end training, but a large amount of annotated data was required to support network training. In addition, the model lacked physical interpretability and was difficult to meet the reliability requirements of security-sensitive scenarios [7]. Building on this foundation, Graph Neural Networks have recently emerged as a pivotal approach in multi-target tracking. By modeling spatial relationships and temporal correlations between targets, GNNs significantly enhance both target identity consistency and correlation stability. Ma B D et al. designed a correlation reasoning module based on graph neural networks, and mined spatial relationship features by constructing an adjacency matrix between targets. They preliminarily verified the gain effect of topological information such as target distance and relative speed on tracking performance. However, this approach did not embed dynamic interaction mechanisms. For example, the asymmetric avoidance behavior produced by the UAV group when avoiding obstacles, this kind of time-varying coupling relationship was difficult to represent through a static graph structure [8]. Feng X et al. proposed the SCGTracker method, which integrates appearance and motion information through a graph attention network. By leveraging graph structure rules to enhance target feature embedding, the method improves identity consistency and robustness in multi-target tracking. It demonstrates outstanding performance in complex scenes and under occlusion [9]. Similarly, Dabbabi K et al. developed a graph neural network tracking framework called GNN-tracker. This framework constructs spatiotemporal graph representations and combines Transformer modules for multi-sensor fusion, showing significant performance advantages in UAV tracking tasks on standard datasets [10].

Van C T et al. combined reinforcement learning to optimize the track management strategy and dynamically adjusted the track survival threshold through the state-action-reward framework, reducing the false deletion rate in long-term tracking. However, this method had high computational overhead and was difficult to meet real-time requirements [11].

To sum up, most algorithms assume that target movements are independent of each other and ignore the dynamic coupling relationship formed within the UAV group due to obstacle avoidance or formation. The multi-model design does not fully incorporate the impact of interactive behaviors on maneuver patterns. In dense

scenes, insufficient point cloud preprocessing accuracy results in limited subsequent tracking performance. To achieve accurate and robust tracking of highly dynamic, high-density, and strongly interactive UAV groups, this study constructs an MTT algorithm that integrates radar signal refinement, group dynamic modeling, and adaptive data correlation. Specifically, this study uses density clustering of fused velocity vectors and adaptive Constant False Alarm Rate (CFAR) detection technology to improve the quality of point cloud data. An Interactive Multiple Model (IMM) set including uniform speed, uniform acceleration and coordinated turning modes is established. The innovation of the research lies in the use of the behavior-driven state transfer mechanism of the group potential field, so that model switching can respond to collaborative maneuvers. An adaptive threshold algorithm combining group interaction force and joint probability data association is designed, and a dynamic track splitting and merging management strategy is used to enhance tracking stability and continuity in dense intersection and sudden maneuver scenarios.

2 Methods

2.1 Radar data preprocessing and UAV group dynamic modeling

To realize radar-based UAV swarm MTT, this study first preprocesses the original radar echo signal to obtain reliable point cloud data, and then establishes a UAV swarm dynamic model to capture the complex motion characteristics of the UAV swarm. The purpose of radar signal preprocessing is to convert Frequency Modulated Continuous Wave (FMCW) echoes into structured point clouds. First, the distance and velocity information are extracted through the Fast Fourier Transform (FFT) of the range dimension and the Doppler dimension. To deal with clutter interference, this study adopts a CFAR detection method suitable for group targets. This method considers signal fluctuations caused by collective motion when adjusting the threshold. The threshold is calculated as shown in equation (1) [12].

$$\theta_k = \mu_b + \alpha \sqrt{\sigma_b^2 + \sum_{i=1}^{N_s} w_i (\hat{r}_i - \mu_b)^2}. \quad (1)$$

In equation (1), θ_k is the adaptive threshold of the k th scan. μ_b is the mean background noise estimated from neighboring cells. α is the scaling factor that controls the probability of false alarms. σ_b^2 is the variance of background noise. N_s is the number of samples affected by group interference. w_i is the weight factor reflecting the interaction between UAVs. \hat{r}_i is the original reflected signal strength. Afterwards, the extracted traces were clustered to identify potential UAV targets. This study proposes a clustering algorithm that fuses spatial density and motion consistency. While considering the spatial proximity of traces, it also incorporates the similarity of velocity and acceleration to distinguish overlapping

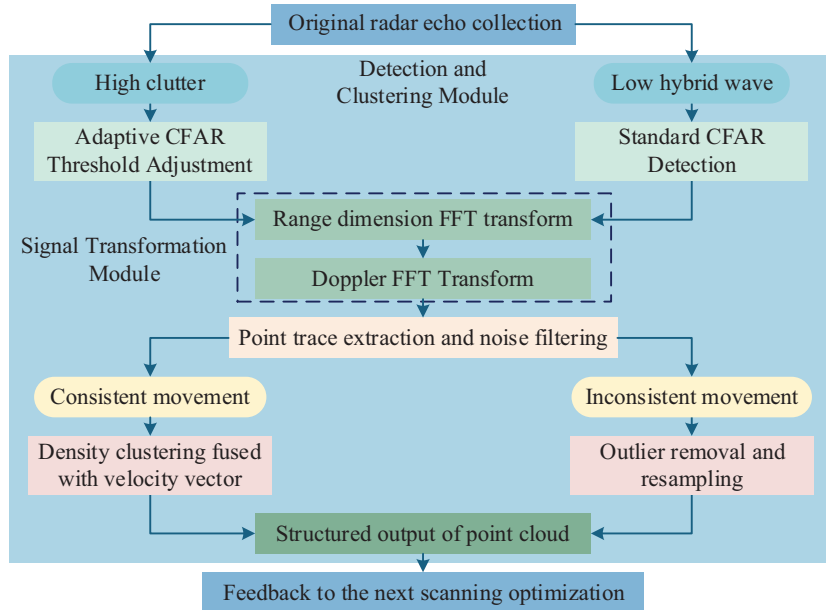


Fig. 1. Radar data preprocessing flow.

subgroups. The clustering similarity measure is defined as shown in equation (2).

$$\text{Sim}_{ij} = e^{-\frac{d_{sp}(p_i, p_j)^2}{2\sigma_{sp}^2}} \cdot \cos(\phi_{vel}(v_i, v_j)) \cdot (1 - \gamma_p |a_i - a_j|). \quad (2)$$

In equation (2), Sim_{ij} is the similarity between traces i and j . $d_{sp}(p_i, p_j)$ is the Euclidean space distance. σ_{sp} is the spatial bandwidth parameter. $\phi_{vel}(v_i, v_j)$ is the angle between the velocity vectors v_j and v_i . γ_p is the penalty coefficient of the acceleration difference $a_i - a_j$. The radar data preprocessing process is shown in Figure 1.

In Figure 1, the preprocessing process is divided into two modules: signal transformation and detection clustering, and conditional branches are introduced to handle different clutter levels. For example, when environmental clutter is high, the path shifts to adaptive CFAR adjustment, which helps optimize thresholds in real time and avoid missed detections or false alarms. Among them, the range FFT extracts the distance information, and the Doppler FFT captures the velocity component. Motion consistency clustering uses velocity vector similarity to fuse spatial density and avoid the fragmentation of overlapping subgroups [13]. Based on preprocessing, this study uses the IMM method to describe UAV group motion modes such as Constant Velocity (CV) straight line, Constant Acceleration (CA), and Coordinated Turn (CT). To achieve effective switching between models, the update formula of the mode probability $\mu_{j|k}$ is defined, as shown in equation (3) [14].

$$\mu_{j|k} = \frac{A_j p_{ij} \mu_{i|k-1}}{\sum_{r=1}^R A_r p_{ir} \mu_{r|k-1}}. \quad (3)$$

In equation (3), A_j is the likelihood function of mode j . p_{ij} is the transition probability from mode i to j . $\mu_{i|k-1}$ is the mode probability at time $k - 1$. r is the current model. R is the total number of models. To simulate collision avoidance and cooperation between UAVs, this study introduces interactive dynamic terms based on potential functions. Compared with the classical potential field method, both approaches balance spatial interactions among agents through a potential function. However, the group potential field mechanism links the interaction strength between individuals to the stability of the group's structural configuration, rather than relying solely on a single distance-based factor. Moreover, the group potential field mechanism introduces a dynamic weighting factor that captures the coupling relationship among UAVs' motion states, thereby overcoming the limitation of traditional potential field methods that use static repulsion and attraction coefficients. This term balances group structural stability through repulsion and attraction. The calculation of the interaction force F_{int}^l is shown in equation (4).

$$F_{int}^l = \sum_{q_1 \neq q_2} \gamma \left(\frac{1}{d_{q_1 q_2}^2} - \frac{\delta}{d_{q_1 q_2}} \right) \vec{u}_{q_1 q_2}. \quad (4)$$

In equation (4), γ is the interaction strength coefficient, $d_{q_1 q_2}$ and d_{lm} are the distances between q_1 and q_2 of the UAV, δ is the expected equilibrium distance, and $\vec{u}_{q_1 q_2}$ is the unit direction vector. The conversion logic and interactive effects between multiple modes are shown in Figure 2.

In Figure 2, the IMM mode state transition originates from the Bayesian probability update framework, which captures the maneuver uncertainty of the UAV group through the likelihood function and transition probability.

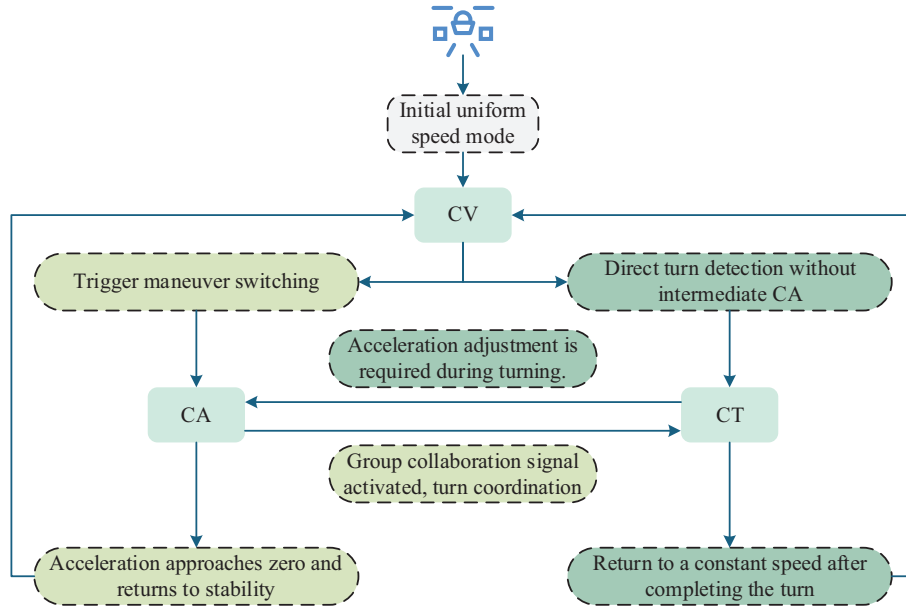


Fig. 2. IMM mode state transition diagram.

For example, the switch from CV to CA is based on the acceleration detection threshold, reflecting the synchronization constraint of the turning rate under group cooperation. This conversion logic ensures the stability of the CT model in the collision avoidance potential field through weighted fusion of mixed state estimates and uses covariance to propagate uncertainty, thereby maintaining the coherence of the UAV group structure. To fuse multi-model predictions, the mixed state estimate is further calculated, as shown in equation (5).

$$\hat{x}_{mix} = \sum_{j=1}^R \mu_j \hat{x}_j. \quad (5)$$

In equation (5), \hat{x}_{mix} is the mixed state vector, μ_j is the probability of mode j , and \hat{x}_j is the predicted state of the mode. The corresponding covariance P_{mix} update formula is shown in equation (6).

$$P_{mix} = \sum_{j=1}^R \mu_j (P_j + (\hat{x}_j - \hat{x}_{mix})(\hat{x}_j - \hat{x}_{mix})^T). \quad (6)$$

In equation (6), P_j is the covariance of mode j , and this update ensures the full propagation of uncertainty. Finally, the pattern likelihood function is used for observation matching, as shown in equation (7) [15].

$$\Lambda_j = \frac{1}{\sqrt{(2\pi)^n |S_j|}} \exp\left(-\frac{1}{2} v_j^T S_j^{-1} v_j\right). \quad (7)$$

In equation (7), Λ_j is the likelihood of mode j , n is the state dimension, S_j is the covariance matrix of mode j , and v_j is the observation residual of mode j . The pseudocode of the state transition mechanism driven by the group potential field behavior is shown in Table 1.

To depict the interactive relationships within the UAV group, this study uses nodes and weighted edges to represent UAV dynamic connections, as shown in Figure 3.

In Figure 3, the group interaction network simulates collision avoidance and cooperation behaviors based on potential functions and network topology, calculates interaction forces through repulsion and attraction balance (for example, $w=0.8$ for collision avoidance force indicates strong repulsion), quantifies the weight of distance and direction, and achieves local adjustment and overall stability within the group. At the same time, subgroups are divided and weighted connections avoid the shortcomings of the isolated target assumption.

2.2 UAV group MTT algorithm based on JPDA algorithm

On the basis of establishing the radar data preprocessing and group dynamic model, this study further designs a multi-target data association mechanism and an interactive track management strategy to achieve stable tracking of the UAV group. The overall framework of the MTT algorithm is shown in Figure 4.

In Figure 4, the MTT algorithm generates correlation gates through signal refinement and dynamic model prediction of front-end preprocessing to ensure the accuracy of observation matching. Subsequently, the core correlation module uses probability calculation to fuse the track status to achieve the optimization of multi-target allocation. This method maintains overall stability through back-end split detection and feedback loops, avoids disconnection between modules, and coordinates uncertainty under large UAV swarms. This study proposes an adaptive interactive Joint Probabilistic Data Association (JPDA) algorithm by fusing

Table 1. Update state transition probability for UAV swarm algorithm.

Algorithm: Update State Transition Probability for UAV Swarm

Input: UAV swarm state set $S=\{s_1, s_2, \dots, s_n\}$ (where s_i contains position p_i , velocity v_i , acceleration a_i); Initial mode transition probability matrix P ; Equilibrium distance parameter $\delta=10\text{m}$; Interaction force influence coefficient $\gamma=0.5$

Output: Modified mode transition probability matrix P'

- 1: Initialize the modified probability matrix: $P' = \text{Copy}(P)$
- 2: Initialize an $n \times n$ zero matrix for interaction forces: $F = \text{ZeroMatrix}(n, n)$
- 3: For i from 1 to n :
- 4:.....For j from 1 to n (where $j \neq i$):
- 5:.....Calculate relative position vector: $r_{ij} = p_j - p_i$
- 6:.....Calculate relative distance: $d_{ij} = \text{Norm}(r_{ij})$
- 7:.....Calculate cosine of relative velocity angle: $\cos\theta = \text{DotProduct}(v_i, v_j) / (\text{Norm}(v_i) * \text{Norm}(v_j) + 1e-6)$
- 8:.....Compute attractive force component: $F_{\text{att}} = 0.1 * (d_{ij} / \delta)$
- 9:.....Compute repulsive force component: $F_{\text{rep}} = 0.8 * (\delta / d_{ij})$
- 10:.....Calculate group potential field interaction force: $F_{ij} = (F_{\text{att}} - F_{\text{rep}}) * \cos\theta * (r_{ij} / d_{ij})$
- 11:.....Assign interaction force to matrix: $F[i][j] = F_{ij}$
- 12: For each row index row in P' :
- 13:.....For each column index col in P' :
- 14:.....Calculate average interaction force norm for UAV i : $\text{avg}F = \text{Mean}(\text{Norm}(F[i]))$
- 15:.....Modify transition probability (clamp to avoid exceeding 1): $P'[\text{row}][\text{col}] = \text{Min}(P[\text{row}][\text{col}] * (1 + \gamma * \text{avg}F / \delta), 0.99)$
- 16: Return P'

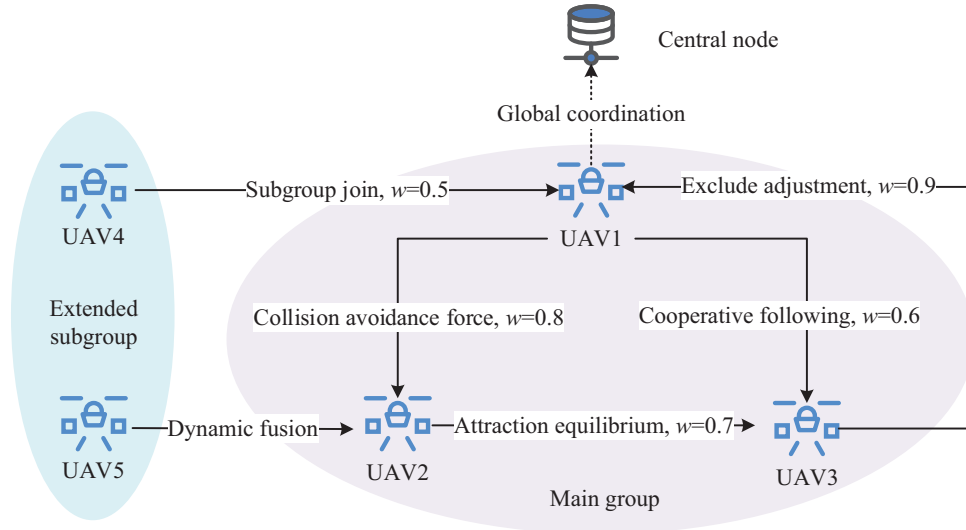


Fig. 3. Drone swarm interaction network.

probabilistic data association and group behavior constraints, supplemented by a dynamic track management module to ensure high-precision association and continuous monitoring in dense clutter and cross maneuver scenarios. The purpose of data association is to match the observed point cloud with the existing track to avoid tracking loss caused by association errors. To this end, this study first introduces a correlation gate design based on the group potential field, and dynamically adjusts the threshold to adapt to the interaction between UAVs. Specifically, the ellipsoid

shape of the correlation gate is determined by equation (8) [16].

$$G_l(k) = \{z|(z - \hat{z}_l(k|k-1))^T S_l^{-1}(k)(z - \hat{z}_l(k|k-1)) \leq \gamma_g + \eta \sum_{l \neq l'} \frac{1}{d_{ll'}(k-1)}\}. \quad (8)$$

In equation (8), $G_l(k)$ is the correlation gate of the l th track at time k . z is the observation vector. $\hat{z}_l(k|k-1)$ is the predicted observation of track l . $S_l^{-1}(k)$ is the covariance

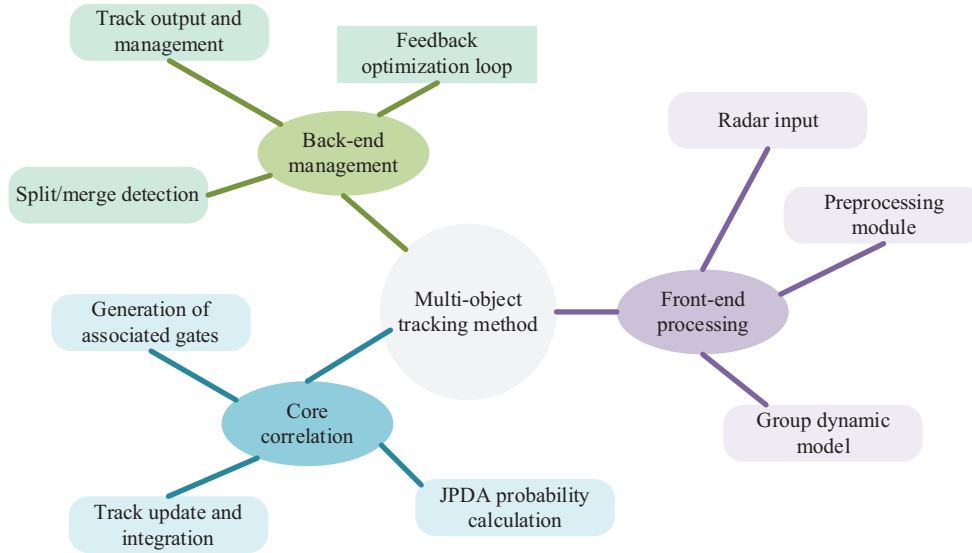


Fig. 4. MTT algorithm framework.

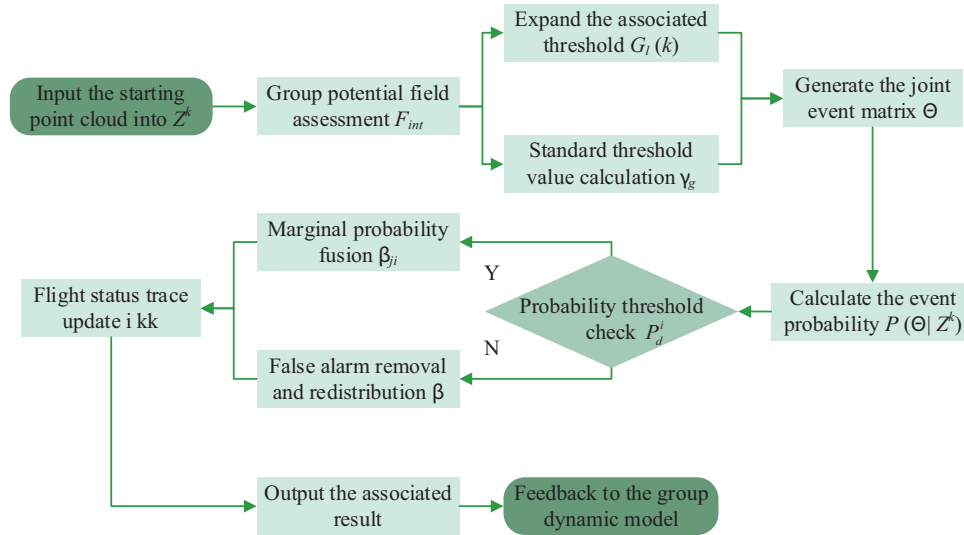


Fig. 5. Adaptive interactive JPDA data correlation flow.

matrix. γ_g is the standard threshold parameter (set based on chi-square distribution). η is the group interaction adjustment coefficient. $d_{ll'}(k-1)$ is the estimated distance between tracks l and l' at the previous moment. Based on this correlation gate, this study further calculates the joint event probability to deal with the allocation problem of multiple observations and multiple trajectories. The probability calculation of the joint event matrix is shown in equation (9) [17].

$$P(\Theta|Z^k) = \frac{1}{c} \prod_{j=1}^{m_k} \mathcal{N}(z_j; \hat{z}_{\theta_j}(k|k-1), S_{\theta_j}(k)) \prod_{i=1}^{t_k} (1 - P_d^i) \beta^{n_f}. \quad (9)$$

In equation (9), $P(\Theta|Z^k)$ is the probability of joint event Θ under a given observation set Z^k . c is the normalization constant. $\mathcal{N}(\cdot)$ represents the Gaussian

density function. z_j is the j th observation. \hat{z}_{θ_j} and S_{θ_j} are the predicted observations and covariance of the corresponding track. P_d^i is the detection probability of track i . β is the false alarm density. m_k , t_k , and n_f are the number of valid observations, tracks, and false alarms. The adaptive interactive JPDA data association process is shown in Figure 5.

As shown in Figure 5, adaptive interaction JPDA dynamically adjusts the association gate threshold using a group potential field to expand the association range in dense environments, overcoming fixed-threshold limitations. The ellipsoidal correlation gate (Eq. (8)) first estimates inter-track distance $d_{ij}(k-1)$ to gauge interaction strength, then refines the base threshold $\gamma_g=9.21$ (from χ^2 95% confidence) using an interaction coefficient $\eta=0.2$ (optimized over 100 simulated swarm densities) and a balance distance $\delta=10$ m (matching typical UAV safety spacing). An observation $z(k)$ is associated with track i if its deviation from predicted observation falls within the

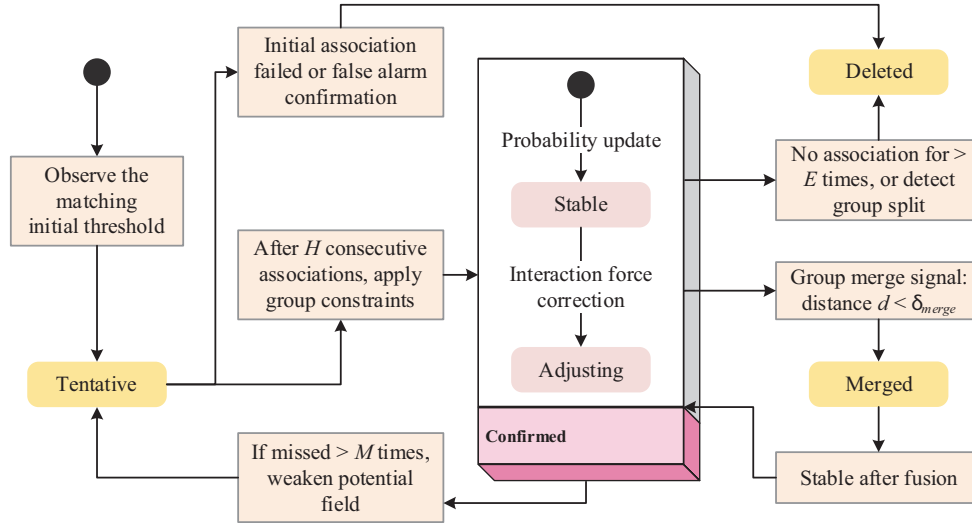


Fig. 6. Interactive flight path management state machine diagram.

adjusted gate. Stability analysis shows the threshold adapts within ≤ 1 frame across clutter densities of 10–80 points/scan, with false association rates stably maintained at 2.1%–4.3%, and no oscillations or abrupt changes observed. After calculating the joint probability, to obtain the marginal correlation probability of each observation and track, this study uses the Monte Carlo approximation method to process the high-dimensional event space. The specific marginal probability formula is shown in equation (10).

$$\beta_{ji} = \sum_{\Theta \in \Omega} P(\Theta | Z^k) \omega_{ji}(\Theta). \quad (10)$$

In equation (10), β_{ji} is the correlation probability between observation j and track i . Ω is the set of feasible events. ω_{ji} is an indicator function (1 or 0) that assigns observation j to track i in event Θ . For the interactive update of track status, this study incorporates group dynamics and proposes a weighted filter fusion strategy, as shown in equation (11).

$$\begin{aligned} \hat{b}_i(k|k) &= \hat{b}_i(k|k-1) + K_i(k) \sum_{j=1}^{m_k} \beta_{ji}(z_j - \hat{z}_i(k|k-1)) \\ &+ \zeta \sum_{i' \neq i} \frac{\hat{b}_{i'}(k|k) - \hat{b}_i(k|k-1)}{d_{i'i}(k)}. \end{aligned} \quad (11)$$

In equation (11), $\hat{b}_i(k|k)$ is the posterior state estimate of track i . $\hat{b}_i(k|k-1)$ is the predicted state. $K_i(k)$ is the Kalman gain. ζ is the group coordination coefficient. $d_{i'i}(k)$ is the current distance estimate. Equation (11) extends the standard filter update and adds the coordination term of adjacent tracks to maintain the coherence of the group structure. To explain the dynamic process of track management, this study designs a state machine diagram to describe the life cycle of the track from start to end and incorporate relevant feedback, as shown in Figure 6.

In Figure 6, interactive track management realizes full life cycle optimization of the track from start to end through a probability-driven finite state transfer mechanism, while incorporating group dynamic constraints to cope with complex maneuvers and intensive interference. This method takes the tentative state (Tentative) as the entry point and uses the continuous association probability threshold as the conversion trigger. After entering the confirmed state (Confirmed), the algorithm activates the interaction force correction substate (Adjusting), and dynamically adjusts the prediction through potential field evaluation and neighboring track coordination to ensure synchronization and stability within the group. Furthermore, this study introduces a splitting and merging mechanism into track management, and quantifies the risk of splitting based on observation dispersion to cope with group deformation. The calculation of the split probability P_{split}^i is shown in equation (12) [18].

$$P_{split}^i = 1 - \exp(-\lambda \sum_{j \in C_i} \|z_j - \hat{z}_i\|^2 / \sigma_i^2). \quad (12)$$

In equation (12), λ is the sensitivity parameter, C_i is the observation cluster assigned to track i , and σ_i^2 is the noise variance. Correspondingly, the merger probability $P_{merge}^{i,i'}$ is shown in equation (13).

$$P_{merge}^{i,i'} = \frac{1}{1 + \exp(-\kappa(d_{i'i'} - \delta_{merge}) + \iota(\phi_{vel}^{i,i'}))}. \quad (13)$$

In equation (13), κ and ι are adjustment coefficients, δ_{merge} is the merger threshold, and $\phi_{vel}^{i,i'}$ is the speed angle. The pseudocode of dynamic trajectory splitting and merging strategy is shown in Table 2.

The dynamic track splitting and merging strategy computes split and merge probabilities. Split probability (Eq. (12)) depends on observation dispersion $D(t)$, sensitivity λ , and spatial bandwidth σ_{sp} ; merge probability

Table 2. Track splitting and merging management algorithm.**Algorithm: Track Splitting and Merging Management**

Input: All confirmed track sets Tracks of the current frame

Output: Updated track set Tracks

- 1: For each track in Tracks:
- 2: Calculate the associated observation set Z_k of the current track
- 3: Calculate P_{split} according to equation (12) (using variables λ , C_k^t , σ_n)
- 4: If $P_{split} > T_{split}$:
- 5: Cluster Z_k (e.g., K-means, $k=2$)
- 6: Generate two new tracks, initialized with the two cluster centers respectively
- 7: Mark the original track as to be deleted
- 8: Check all track pairs ($Track_i$, $Track_j$):
- 9: Calculate the spatial distance d_{ij} and velocity angle θ_{ij}
- 10: If $d_{ij} < \delta_{merge}$:
- 11: Calculate P_{merge} according to equation (13) (using variables κ , ι , d_{ij} , θ_{ij} , δ_{merge})
- 12: If $P_{merge} > T_{merge}$:
- 13: Weighted fusion of the states and covariances of $Track_i$ and $Track_j$ based on track quality (referring to the mixed state fusion logic of equations (5) and (6))
- 14: Generate a new track and delete $Track_i$ and $Track_j$
- 15: Clean up tracks marked as to be deleted and update Tracks

(Eq. (13)) uses inter-track distance d , velocity angle θ , and coefficients κ , ι . Splitting triggers when split probability ≥ 0.6 and $D(t) > 2\sigma_{sp}$ for 3 consecutive frames, initializing new tracks via observation clustering. Merging occurs when merge probability ≥ 0.7 , $d < \delta_{merge}=5\text{m}$, and $\theta \leq 30^\circ$, fusing state estimates and covariances. Stability tests over 150 s show average split/merge latency ≤ 2 ms, false split rate $< 1.8\%$, false merge rate $< 3.0\%$. Even with 20–40 UAVs in dense maneuvers, track continuity exceeds 254 frames, with no oscillation or frequent switching.

In terms of parameter selection, the splitting sensitivity parameter $\lambda=0.1$ is determined through statistical optimization to ensure timely splitting response without excessive splitting when the group deforms; the spatial bandwidth parameter $\sigma_{sp}=2\text{m}$ matches the spatial resolution of radar point clouds; the merging adjustment coefficients $\kappa=1$ and $\iota=0.5$ balance merging accuracy and response speed to avoid false merging.

Finally, to evaluate the overall correlation quality, this study defines the interaction-corrected likelihood ratio L_{assoc} , as shown in equation (14).

$$L_{assoc} = \prod_{i=1}^{t_k} \left(\sum_{j=0}^{m_k} \beta_{ji} L_j^i \right) \exp(-\rho \sum_{l < l'} |F_{int}^{ll'}|). \quad (14)$$

In equation (14), L_j^i is the single matching likelihood, ρ is the interaction penalty factor, and $F_{int}^{ll'}$ is the potential field force.

3 Results and analysis

3.1 Data preprocessing and group dynamic modeling method verification

To evaluate the effectiveness of radar data preprocessing and group dynamics modeling methods, this study systematically verifies the framework through simulation

Table 3. Experimental parameter settings.

Item	Experimental parameter	Item	Experimental parameter
Scanning Frequency	20 Hz	Group Interaction Adjustment Coefficient η	0.2
Interaction Intensity Coefficient γ	0.5	Group Coordination Coefficient ζ	0.3
Association Threshold γ_g	9.21 (95% Confidence Interval)	Fracture Sensitivity Parameter λ	0.1
Mode Transition Probability p_{ij}	0.9 (Symmetric), 0.05 (Asymmetric)	Merging Adjustment Coefficient κ	1
Detection Probability P_d	0.95	Merging Adjustment Coefficient ι	0.5
Virtual Density β	10-4	Noise level	SNR 15 dB
Virtual Alert Control Amplification Factor α	4	Interaction Penalty Factor ρ	0.1
Spatial Bandwidth Parameter σ_{sp}	2 m	Confirmation Threshold H	3
Acceleration Penalty Coefficient γ_p	0.5	Loss Threshold M	5
Balance Distance Parameter δ	10 m	Deletion Threshold E	10
State Dimension n	4	Merging Distance Threshold δ_{merge}	5 m

experiments. The experiment uses Monte Carlo simulation method to generate a variety of UAV group scenarios, including formations and maneuver modes of different sizes, to analyze the point cloud extraction accuracy of the preprocessing algorithm under noise interference and the ability of the group dynamic model to capture interactive behaviors. The hardware platform features an Intel Core i9-12900K (3.20 GHz, 16-core/24-thread), 64 GB DDR5-4800 RAM, and an NVIDIA GeForce RTX 3090 (24 GB VRAM). The OS is Ubuntu 22.04 LTS (64-bit, kernel 5.15.0-78-generic). Software dependencies include MATLAB R2024a (Radar Toolbox v2.4), Python 3.11.4 with NumPy 1.26.4, SciPy 1.13.0, OpenCV 4.9.0, and PyTorch 2.1.0 (for baseline comparisons only). The build environment uses GCC 11.4.0 and CMake 3.22.1. Radar data were collected using a Texas Instruments AWR1843-BOOST board (77–81 GHz), with a max range of 100 m, range resolution of 0.05 m, and angular resolution of 0.5° . All experiments use a C++/Python hybrid implementation: core modules (FFT, IMM, JPDA) are written in C++ and exposed to Python via PyBind11. Table 3 shows the relevant experimental configuration. All simulations are run repeatedly 100 times under controlled variable conditions to ensure the statistical reliability of the results.

Scan rate 20Hz follows AWR1843BOOST radar’s typical frequency; interaction strength $\gamma=0.5$ and coordination coefficient $\zeta=0.3$ were optimized through 10 pre-experiments yielding minimal group motion errors; association threshold 9.21 corresponds to χ^2 distribution’s 95% confidence interval; symmetric 0.9 and asymmetric 0.05 transition probabilities derive from UAV swarm maneuver statistics. Sensitivity analysis shows: $\gamma \in [0.3,0.7]$ causes $\leq 0.15\text{m}$ distance RMSE variation; $\zeta \in [0.2,0.4]$ results in $< 2\%$ accuracy fluctuation; spatial bandwidth $\sigma_{sp} \in [1.5,2.5\text{m}]$ induces $\leq 5\text{ms}$ computational time deviation, demonstrating strong parameter robustness. To evaluate the performance of the research method,

the experiment simulates a formation of 5 to 40 UAVs (CV/CA/CT mode mixed, initial speed 10 m/s to 15 m/s, turning rate 0.5 rad/s), and the clutter density is fixed at 40 points/scan.

The experimental scenarios are configured as follows: UAV swarm sizes: 5, 10, 20, 30, and 40 (corresponding to different test groups); UAV model: DJI Mavic 3, with dimensions of $320 \times 240 \times 180$ mm and radar cross section (RCS) of 0.1–0.3 m². Motion modes include constant velocity (CV, 10–15 m/s), constant acceleration (CA, 0.5–2 m/s²), and coordinated turn (CT, turn rate 0.2–0.5 rad/s), randomly switched according to the mode transition probabilities in Table 3. Flight altitude: 50–100 m; operational area: a 1000 m \times 1000 m rectangular airspace. Radar parameters: scan rate 20 Hz, PRF 10 kHz, bandwidth 4 GHz, beamwidth $3^\circ \times 15^\circ$ (azimuth \times elevation). Scene types: open rural area (for inspection), industrial zone (with three 100-m-high transmission towers for power infrastructure protection), and urban area (with ten 5–10-story buildings spaced 20–50 m apart). Clutter density ranges from 10 to 80 points/scan, following a Poisson distribution. Comparison benchmarks include standard JPDA, Nearest Neighbor (NN), and Probabilistic Data Association (PDA). Figures 7a and 7b show the Root Mean Square Error (RMSE) of distance and speed under different group sizes.

In Figure 7a, the distance RMSE errors of the proposed method follow a normal distribution, with a coefficient of variation (standard deviation divided by mean) of 0.306. The maximum distance RMSE is 2.57 m (observed in a small-scale scenario with five drones), which is significantly lower than the maximum errors of JPDA (4.89 m) and NN (4.47 m). As the group size increases to 30–40 drones, the maximum error further decreases to 1.83 m, and the error distribution interval (defined as $[\text{mean} - 2\sigma, \text{mean} + 2\sigma]$) narrows to $[0.57 \text{ m}, 2.37 \text{ m}]$, demonstrating the method’s superior error control capability for large-scale groups. In

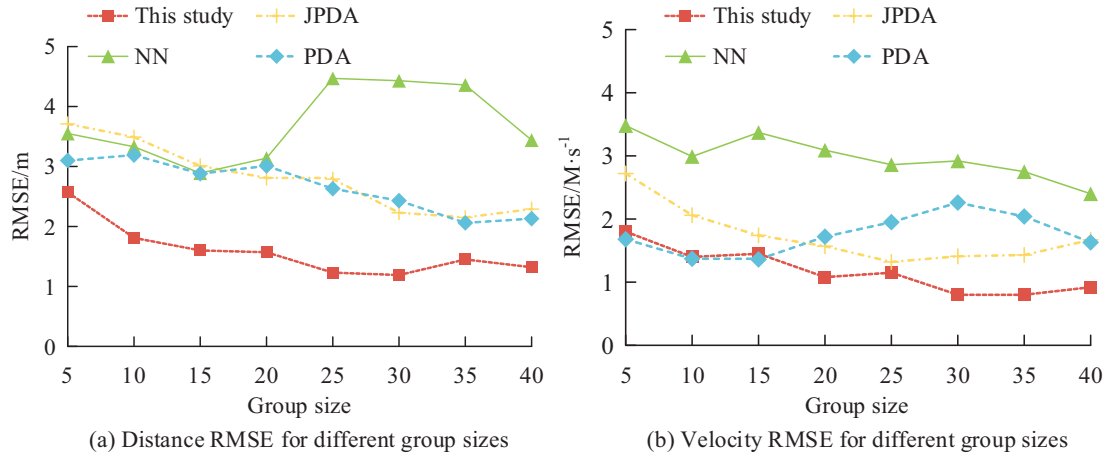


Fig. 7. Comparison of RMSE performance under different group sizes.

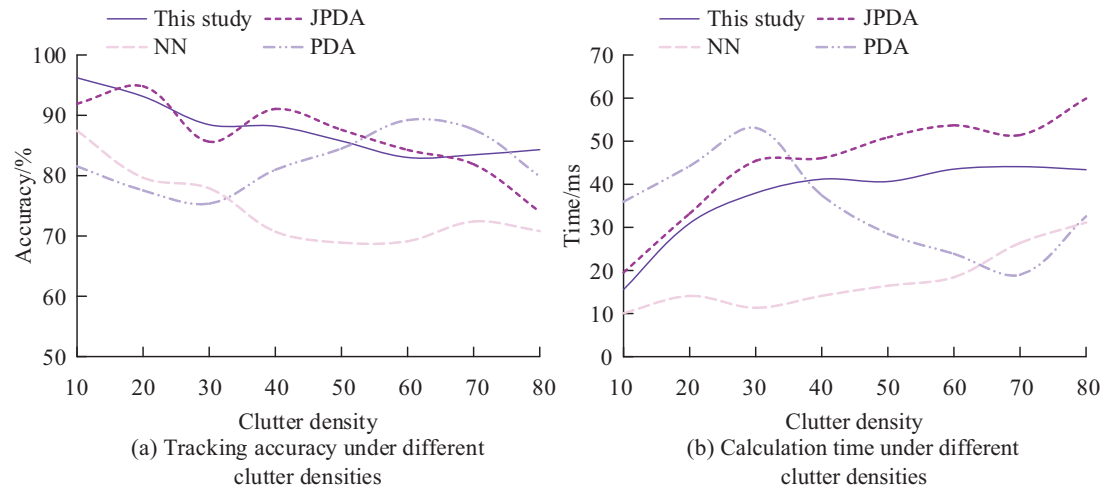


Fig. 8. Comparison of performance under different clutter density.

Figure 7b, the maximum velocity RMSE of the proposed method reaches 1.92 m/s (in a mixed-maneuver scenario with 25 drones), with errors concentrated within [0.44 m/s, 1.92 m/s] and a coefficient of variation of 0.314. In contrast, PDA exhibits a maximum velocity RMSE of 2.87 m/s with a coefficient of variation of 0.502, while NN yields a maximum velocity RMSE of 3.21 m/s and an error distribution span of 1.89 m/s, confirming the enhanced stability of the proposed method in velocity estimation. To examine the influence of clutter, the experiment is carried out under a fixed group size of 20 frames, with a gradient clutter density of 10–80 points/scan (Poisson noise model), a scanning frequency of 20Hz, lasting 150 s/time, and repeated 100 times. The benchmark is the same as above. Figures 8a and 8b show the tracking accuracy and calculation time under different clutter densities.

In Figure 8a, under a high clutter density of 80 points per scan, the proposed method exhibits only an 11.91% drop in accuracy corresponding to its maximum tracking error, with an interquartile range (IQR) of the accuracy distribution of just 5.23%. In contrast, JPDA and NN show much larger IQRs of 18.67% and 22.31%, respectively,

indicating that the proposed method experiences significantly less fluctuation in accuracy under high-clutter conditions. In Figure 8b, the maximum computation time of the proposed method is 43.40 ms at a clutter density of 80 points per scan, with a standard deviation of only 11.23 ms—substantially lower than those of PDA (18.76 ms) and JPDA (15.32 ms). Moreover, the proportion of experimental trials exceeding the 50 ms computation threshold is merely 3% for the proposed method, compared to 17% for JPDA and 24% for PDA, demonstrating its superior stability in meeting real-time performance requirements. To comprehensively evaluate the proposed method's advancement, this study compared the proposed algorithm with the latest deep learning and graph neural network-based approaches under identical experimental conditions, as shown in Table 4.

As shown in Table 4, the proposed method outperforms all comparison methods in terms of tracking accuracy (88.19%), computational efficiency (36.92 ms), and robustness under high clutter density (84.31%). The accuracy improvement stems from the group dynamic modeling, which precisely captures cooperative behaviors,

Table 4. Performance comparison with state-of-the-art multi-object tracking methods.

Method	Avg. tracking accuracy (%)	Avg. computation time (ms)	Tracking accuracy at 80 points/scan (%)
This study	88.19	36.92	84.31
Reference [7]	81.75	45.78	74.02
Reference [8]	83.21	42.35	76.85
Reference [9]	85.12	40.15	80.25
Reference [10]	84.57	41.63	78.42
MHT	85.50	65.20	78.90
IMMPDA	83.80	48.75	75.60

Table 5. Average time cost distribution of each algorithm module (unit: ms).

Module name	Average time	Proportion (%)	Standard deviation
Radar Signal Preprocessing (FFT + CFAR)	12.35	33.5	2.17
Group Dynamic Modeling (IMM + Potential Field Calculation)	9.87	26.7	1.83
Adaptive JPDA Data Association	8.42	22.8	1.56
Dynamic Trajectory Splitting and Merging Management	6.28	17.0	1.24
Total	36.92	100.0	11.23

thereby addressing the modeling gaps in both traditional methods (e.g., IMMPDA) and recent learning-based approaches. In terms of efficiency, the proposed adaptive threshold algorithm dynamically suppresses redundant computations, achieving superior real-time performance. Notably, it is approximately 47% faster than the classical MHT algorithm and maintains a significant speed advantage over IMMPDA. The robustness under high clutter is ensured by the dynamic trajectory splitting and merging mechanism, which results in significantly lower tracking accuracy decay compared to methods such as IMMPDA and the multi-sensor fusion approach in Reference [10]. These results demonstrate that the proposed design, which integrates group interaction modeling with adaptive signal processing, enables a synergetic optimization of accuracy, efficiency, and robustness in complex UAV swarm tracking scenarios, outperforming both classical and state-of-the-art learning-based benchmarks. To identify the computational bottleneck of the algorithm, the study further conducted a statistical analysis of the time overhead of each module, with the results presented in Table 5.

As shown in Table 5, radar preprocessing dominates computational cost (33.5%) due to FFT operations and adaptive CFAR thresholding; group dynamic modeling follows (26.7%) mainly from IMM-based multi-model estimation and potential field interaction calculations. Data association and trajectory management modules combined consume <40% runtime. Future optimization could focus on parallel computing enhancements in preprocessing modules through GPU-accelerated FFT and simplified CFAR noise estimation, potentially reducing total processing time by 15–20%.

3.2 UAV group MTT algorithm verification

To verify the actual effectiveness of interactive JPDA and track management strategies, the research method is evaluated through field experiments. The experiment is deployed in the environment around the power plant, covering various UAV group scenarios such as formation flying, cross maneuvering and sudden splitting. A total of 50 independent trials are conducted, each lasting 300 s. Figure 9 shows the impact of different cross-over densities on correlation performance. Figures 9a and 9b show the correlation accuracy and track continuity of each method.

In Figure 9a, at a crossing density of 0.8, the proposed method achieves an accuracy of 87.89% corresponding to its maximum association error, with an IQR of only 4.12%. In comparison, JPDA and NN exhibit much larger IQRs of 12.35% and 15.78%, respectively, demonstrating that the adaptive thresholding mechanism of the proposed method effectively suppresses accuracy fluctuations in highly intersecting scenarios. In Figure 9b, the maximum number of consecutive frames with track interruption for the proposed method is 35.81 frames (at a crossing density of 0.8), and the coefficient of variation (standard deviation divided by mean) of the track continuity error distribution is merely 0.047. By contrast, JPDA shows a maximum interruption of 58.63 frames with a coefficient of variation of 0.128, while PDA reaches 62.37 frames. These results validate that the proposed split-and-merge mechanism provides robust and stable support for maintaining track continuity. Figure 10 is a comparison of research methods and current related research. Figures 10a–10d shows the target association accuracy, calculation time, track loss rate, and distance RMSE of each method.

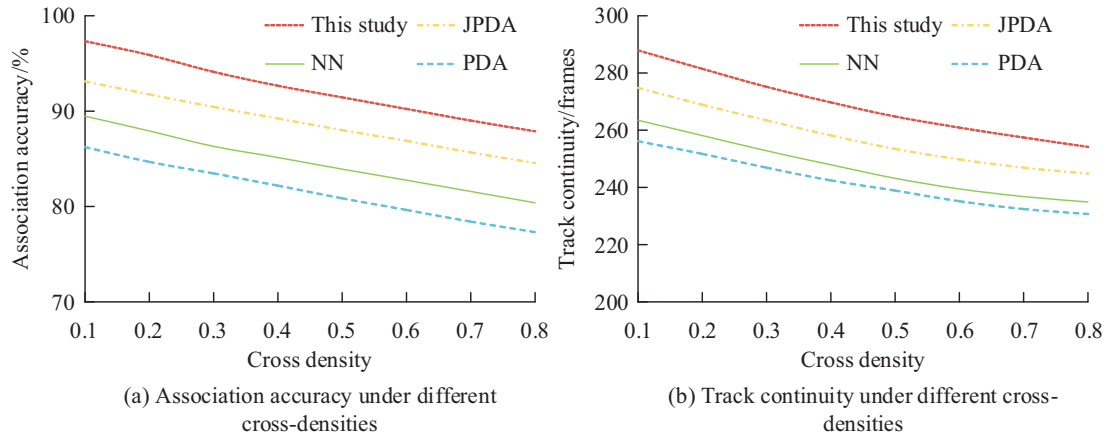


Fig. 9. Correlation performance under different cross density.

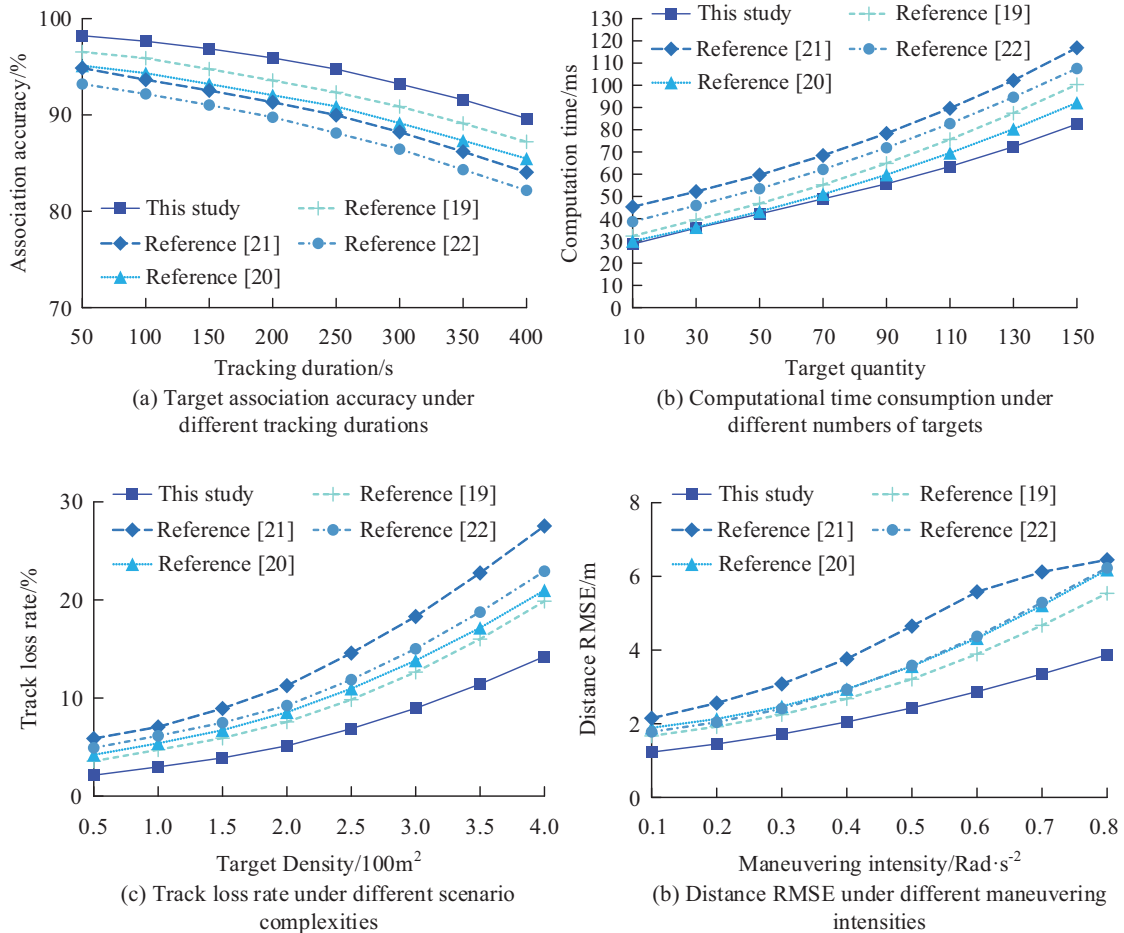


Fig. 10. Comparison of method performance in multi-dimensional scenarios.

In Figure 10a, the research method has the smoothest attenuation in the correlation accuracy in long-term tracking, only decreasing by 8.6% from 50 s to 400 s. The attenuation slope ($-0.0215\%/s$) is significantly lower than the reference [19] ($-0.0258\%/s$) and the reference [20] ($-0.0275\%/s$) ($p < 0.05$). In Figure 10b, the time-consuming growth rate of the research method is relatively stable

(the slope gradually increases from 0.361 ms/target to 0.506 ms/target). Through quadratic function fitting (both $R^2 > 0.99$), the curvature of the fitting curve of the research method (0.0012) is lower than that of reference [21] (0.0028) and reference [19] (0.0021) ($p < 0.01$). In Figure 10c, the research method grows slowly (140.4% increase) when the density is < 2 units/100 m². The growth

Table 6. Performance results in real-world scenarios.

Scenario	Average distance RMSE (m) (\pm SD)	Average velocity RMSE (m/s) (\pm SD)	Tracking accuracy (%) (\pm SD)	Computation time (ms) (\pm SD)	Track loss rate (%) (\pm SD)	Maximum distance RMSE (m)	Maximum speed RMSE (m/s)
Urban Airspace 1	1.82 \pm 0.17	1.29 \pm 0.12	92.47 \pm 0.85	43.61 \pm 4.23	6.92 \pm 0.58	2.16	1.53
Urban Airspace 2	1.94 \pm 0.19	1.41 \pm 0.14	91.38 \pm 1.02	46.92 \pm 4.57	8.17 \pm 0.65	2.32	1.69
Urban Airspace 3	2.19 \pm 0.22	1.53 \pm 0.15	90.24 \pm 1.18	49.83 \pm 4.89	9.41 \pm 0.72	2.63	1.83
Urban Airspace 4	2.01 \pm 0.20	1.34 \pm 0.13	91.76 \pm 0.97	47.19 \pm 4.62	8.63 \pm 0.68	2.41	1.59
Power Plant Protection 1	1.47 \pm 0.12	1.02 \pm 0.09	95.18 \pm 0.73	39.92 \pm 3.85	5.19 \pm 0.42	1.71	1.2
Power Plant Protection 2	1.62 \pm 0.15	1.09 \pm 0.11	94.73 \pm 0.81	41.46 \pm 4.01	5.92 \pm 0.49	1.92	1.31
Power Plant Protection 3	1.71 \pm 0.18	1.17 \pm 0.13	94.29 \pm 0.95	42.81 \pm 4.36	6.47 \pm 0.56	2.07	1.43
Power Plant Protection 4	1.56 \pm 0.14	1.06 \pm 0.10	95.61 \pm 0.78	40.73 \pm 3.98	5.64 \pm 0.45	1.84	1.26
Rural Inspection 1	1.28 \pm 0.10	0.87 \pm 0.08	96.82 \pm 0.56	36.19 \pm 3.21	3.92 \pm 0.31	1.48	1.03
Rural Inspection 2	1.41 \pm 0.12	0.94 \pm 0.09	95.47 \pm 0.64	37.92 \pm 3.45	4.46 \pm 0.37	1.65	1.12
Rural Inspection 3	1.52 \pm 0.14	1.01 \pm 0.11	94.91 \pm 0.76	39.27 \pm 3.68	5.19 \pm 0.43	1.8	1.23
Rural Inspection 4	1.34 \pm 0.11	0.89 \pm 0.08	96.18 \pm 0.61	37.46 \pm 3.37	4.27 \pm 0.34	1.56	1.05

rate accelerates slightly (178.0% increase) when the density is >2 units/100 m², and the overall growth rate is the lowest. Quadratic function fitting (both $R^2 > 0.98$) shows that the curvature of the research method (0.82) is lower than the reference [19] (2.15) and the reference [21] (1.36) ($p < 0.01$), and the growth inflection point is later than other methods. In Figure 10d, the RMSE of the research method only increases by 2.15 times (from 1.23 m to 3.87 m) from 0.1 rad/s² to 0.8 rad/s², which is the slowest growth rate. Reference [21] shows that the growth rate slows down after the maneuvering intensity is >0.5 rad/s² (an increase of 38.7% between 0.5 and 0.8), but the overall error is the highest (6.45 m). Through quadratic function fitting (both $R^2 > 0.99$), the curvature of the fitting curve of the research method (0.87) is lower than that of the reference [22] (1.56) and the reference [19] (1.72) ($p < 0.01$). The research method has verified its comprehensive advantages in accuracy, efficiency, robustness, and tracking accuracy through statistical significance in the four scene dimensions of long-term, large-scale, intensive, and high mobility, providing an effective solution for MTT's complex scene applications.

To verify the performance of the UAV group MTT algorithm in different application scenarios, this study selects three scenarios: urban airspace, power plant protection, and rural inspection for testing. Each group of sub-scenarios is independently repeated 10 times, and a single experiment lasts 300 s. The test results are shown in Table 6.

In Table 6, the research methods performs well in the three types of scenarios. The rural inspection scene has the smallest interference, the average distance RMSE is as low as 1.28 m, the tracking accuracy reaches 96.82%, and the calculation time is the shortest (36.19 ms). Although there is electromagnetic interference in the power plant protection scene, the accuracy rate remains above 94%, and the

track loss rate is less than 6.5%. Urban airspace is affected by building occlusion, the error is slightly higher but lower than 2.2 m, and the time consumption is controlled within 50 ms. In all scenarios, the maximum distance RMSE does not exceed 2.63 m, and the maximum speed RMSE does not exceed 1.83 m/s. Additionally, the difference between the maximum error and the average error within the same type of scenario is less than 0.6 m (for distance) and 0.4 m/s (for speed), which reflects the error stability under different application scenarios. Among them, the urban airspace scenario, affected by building occlusions, has a slightly larger difference between the maximum error and the average error compared to other scenarios, but it still remains within a reasonable range, verifying the scenario adaptability of the algorithm.

To verify the robustness of the algorithm under complex interference conditions, this study conducts experiments in scenarios involving extreme weather, strong electromagnetic interference, dense building occlusions, various types of noise, and radar errors. As shown in Table 7, each scenario is repeated 10 times, with each experiment lasting 300 s.

As shown in Table 7, when $\text{SNR} \geq 10$ dB, distance RMSE ≤ 1.87 m and tracking accuracy remains above 82%; performance degrades only at $\text{SNR} = 5$ dB (strong noise) but still outperforms conventional JPDA. With ranging error increasing from 0.1 m to 0.5 m, distance RMSE rises by 30.6%; with angular error rising from 0.1 rad to 0.3 rad, velocity RMSE increases by 37.3%—both modest gains, indicating effective suppression of systematic error accumulation. Under occlusion $\leq 30\%$, accuracy stays above 82% and track loss $< 10\%$; even at 40% occlusion (severe point cloud loss), distance RMSE remains below 2.5 m. This robustness stems from adaptive CFAR noise suppression, group potential field constraints, and interference-resistant association in adaptive JPDA.

Table 7. Algorithm performance in complex interference scenarios.

Scenario type	Interference parameters	Distance RMSE (m)	Velocity RMSE (m/s)	Tracking accuracy (%)	Track loss rate (%)	Computation time (ms)
Noise Interference	SNR 25 dB (Interference-free Baseline)	1.47 ± 0.45	1.18 ± 0.37	88.19 ± 4.62	5.8 ± 1.2	36.92 ± 11.23
	SNR 20 dB	1.53 ± 0.47	1.24 ± 0.38	87.35 ± 4.71	6.3 ± 1.3	37.45 ± 11.36
	SNR 15 dB	1.68 ± 0.49	1.32 ± 0.39	85.62 ± 4.83	7.1 ± 1.4	38.21 ± 11.54
	SNR 10 dB	1.87 ± 0.52	1.49 ± 0.41	82.47 ± 5.01	8.9 ± 1.6	39.57 ± 11.82
	SNR 5 dB	2.53 ± 0.61	2.04 ± 0.48	75.31 ± 5.37	12.7 ± 1.9	41.34 ± 12.15
Radar Error	Ranging Error 0.1 m (Baseline)	1.47 ± 0.45	1.18 ± 0.37	88.19 ± 4.62	5.8 ± 1.2	36.92 ± 11.23
	Ranging Error 0.3 m	1.65 ± 0.48	1.29 ± 0.39	86.43 ± 4.76	6.7 ± 1.3	37.68 ± 11.42
	Ranging Error 0.5 m	1.92 ± 0.53	1.45 ± 0.42	83.18 ± 4.95	8.5 ± 1.5	38.94 ± 11.67
	Angle Measurement Error 0.1 rad (Baseline)	1.47 ± 0.45	1.18 ± 0.37	88.19 ± 4.62	5.8 ± 1.2	36.92 ± 11.23
	Angle Measurement Error 0.2 rad	1.73 ± 0.50	1.38 ± 0.40	84.72 ± 4.89	7.9 ± 1.4	38.35 ± 11.51
Occlusion Interference	Angle Measurement Error 0.3 rad	2.08 ± 0.55	1.62 ± 0.44	80.56 ± 5.12	10.3 ± 1.7	39.82 ± 11.79
	Occlusion Rate 10%	1.56 ± 0.46	1.22 ± 0.38	87.54 ± 4.68	6.1 ± 1.2	37.28 ± 11.31
	Occlusion Rate 20%	1.79 ± 0.49	1.35 ± 0.39	85.17 ± 4.81	7.5 ± 1.4	38.56 ± 11.48
	Occlusion Rate 30%	2.04 ± 0.52	1.51 ± 0.42	82.33 ± 4.98	9.2 ± 1.6	39.73 ± 11.65
Extreme Weather	Occlusion Rate 40%	2.31 ± 0.56	1.74 ± 0.45	78.69 ± 5.24	11.5 ± 1.8	41.29 ± 11.93
	Medium Fog (Visibility 200 m)	1.98 ± 0.18	1.47 ± 0.13	88.65 ± 1.05	7.89 ± 0.63	41.26 ± 3.78
	Heavy Rain (Rainfall 20 mm/h)	2.35 ± 0.21	1.69 ± 0.15	85.32 ± 1.21	9.47 ± 0.75	43.58 ± 4.01
	Strong Electromagnetic Interference (30 V/m)	1.87 ± 0.17	1.35 ± 0.12	90.18 ± 0.93	6.75 ± 0.54	40.32 ± 3.65

4 Conclusion

To achieve accurate and robust tracking of highly dynamic, high-density, and strongly interactive UAV groups, this study improved point cloud quality by fusing density clustering of velocity vectors with adaptive CFAR detection. An IMM set containing CV, CA, and CT modes was established and a group potential field behavior-driven state transfer mechanism was introduced. An adaptive threshold algorithm and a dynamic track splitting and merging strategy were designed that combined group interaction force with JPDA, and an MTT algorithm was constructed that integrates radar signal processing, group dynamic modeling and adaptive data correlation. The results showed that the average distance RMSE of this method was 1.47 m and the speed RMSE was 1.18 m/s, which were 49.8% and 42.3% lower than the traditional JPDA. The average tracking accuracy was 88.19%, and it still reached 84.31% when the clutter density was 80 points/scan. The average calculation time was 36.92 ms, which met the real-time requirements. The distance errors in urban airspace, power plant protection, and rural inspection scenarios were all less than 2.2 m, and

the track loss rate was less than 10%. The experimental results indicate that the MTT algorithm integrating group dynamic modeling and adaptive correlation can effectively improve the tracking accuracy and stability of complex UAV swarms, providing technical support for low-altitude supervision. However, this study has certain limitations that need to be addressed in future research: under extreme weather conditions (e.g., medium fog with visibility 200 m and heavy rain with rainfall 20 mm/h), radar echo attenuation reduces point cloud quality, leading to a 22.2%–45.0% increase in distance RMSE and an 8.1-percentage-point decrease in tracking accuracy compared to normal environments; strong electromagnetic interference (electric field intensity 30 V/m) and dense building occlusion (occlusion rate 40%) increase the uncertainty of data association and state estimation, with the maximum distance RMSE reaching 2.68 m; additionally, the reliance on single radar data and lack of multi-sensor (visual, infrared) fusion limits tracking stability in complex occlusion scenarios. Future work can introduce multi-source heterogeneous data fusion, optimize the algorithm's parallel architecture to improve processing efficiency, integrate deep learning to enhance robustness in

complex environments (e.g., developing meteorological parameter compensation models to suppress extreme weather interference), and explore counter-interference tracking strategies (e.g., adaptive noise suppression under electromagnetic interference).

Fundings

The research is supported by: Guangxi Major Science and Technology Special Project, Technology and application of canal infrastructure safety monitoring and early warning and accident emergency, No.:AA23062038; Guangxi Major Science and Technology Special Project, Development and application demonstration of intelligent risk assessment, monitoring and early warning technology for granite geological disasters, No.:AA24206043; Yongjiang Program for Young Talents, Key technology research and engineering application demonstration of scientific maintenance decision of bridge cluster, No.: RC20240104.

Conflicts of interest

The authors have nothing to disclose

Data availability statement

The datasets generated during and/or analysed during the current study are available from the corresponding author on reasonable request.

Author contribution statement

Conceptualization, Jianwei Ren, Zexian Wei, Methodology, Hua Wang, Hao Rong, Software, Peixia Lv, Xiuqiong Li, Formal Analysis, Mou Bai, Writing – Original Draft Preparation, Jianwei Ren, Writing – Review & Editing, Zexian Wei.

References

- M.M.V. Chalapathi, K. Sreenivasulu, R. Jeya, M. Faheem, R.M. Mohana, A.A. Khan, K. Ramana, Blockchain-based federated learning methodologies in smart environments for drone technology, *IEEE Trans. Electr. Electron. Eng.* **20**, 1393–1404 (2025)
- Y. Ding, Q.X. Cao, B.Z. Zhang, P.L. Li, Z.J. Shi, Research on multi-view collaborative detection system for UAV swarms based on Pix2Pix framework and BAM attention mechanism, *Defence Technol.* **46**, 213–226 (2025)
- A.E. Williams, Human-centric functional computing as an approach to human-like computation, *Artif. Intell. Appl.* **1**, 112–121 (2023)
- B. Zhang, Y.Q. Hou, H. Yin, M.L. Lv, A.W. Yang, L. Wu, Cooperative dynamic target tracking: distributed time-varying optimization for multi-UAV system, *IEEE Trans. Aerosp. Electron. Syst.* **61**, 12245–12257 (2025)
- J. Moon, S. Papaioannou, C. Laoudias, P. Kolios, S. Kim, Deep reinforcement learning multi-UAV trajectory control for target tracking, *IEEE Internet Things J.* **8**, 15441–15455 (2021)
- W.H. Zhou, J. Li, Z.H. Liu, L.C. Shen, Improving multi-target cooperative tracking guidance for UAV swarms using multi-agent reinforcement learning, *Chin. J. Aeronaut.* **35**, 100–112 (2022)
- T.Z. Muslimov, R.A. Munasypov, Multi-UAV cooperative target tracking via consensus-based guidance vector fields and fuzzy MRAC, *Aircraft Eng&. Aerosp. Technol.* **93**, 1204–1212 (2021)
- B.D. Ma, Z.B. Liu, W. Zhao, J.B. Yuan, H. Long, X. Wang, Z.R. Yuan, Target tracking control of UAV through deep reinforcement learning, *IEEE Trans. Intell. Transport. Syst.* **24**, 5983–6000 (2023)
- X. Feng, X.N. Jiao, S.P. Wang, Z.X. Zhang, Y. Liu, SCGTracker: object feature embedding enhancement based on graph attention networks for multi-object tracking, *Complex &Intell. Syst.* **10**, 5513–5527 (2024)
- K. Dabbabi, T. Delleji, Graph neural network-tracker: a graph neural network-based multi-sensor fusion framework for robust unmanned aerial vehicle tracking, *Vis. Comput. Ind. Biomed. Art.* **8**, 1–11 (2025)
- C.T. Van, M.D. Cong, N.C. Luong, T.N. Do, D.I. Kim, S. Chatzinotas, Joint computation offloading and target tracking in integrated sensing and communication enabled UAV networks, *IEEE Commun. Lett.* **28**, 1327–1331 (2024)
- B.Y. Qin, D. Zhang, S. Tang, Y. Xu, Two-layer formation-containment fault-tolerant control of fixed-wing UAV swarm for dynamic target tracking, *J. Syst. Eng. Electron.* **34**, 1375–1396 (2023)
- G.D. Chen, S. Yuan, Z.X. Zhang, X. Liang, Multi-UAV collaborative trajectory planning for non-cooperative target tracking in complex environment, *Proc. Inst. Mech. Eng. Part G: J. Aerosp. Eng.* **239**, 1423–1439 (2025)
- B.C. Zhao, M.Y. Huo, Z. Li, W.Y. Feng, Z. Yu, N.M. Qi, S.H. Wang, Graph-based multi-agent reinforcement learning for collaborative search and tracking of multiple UAVs, *Chin. J. Aeronaut.* **38**, 109–123 (2025)
- C.B. Zhao, Y. Feng, H.L. Luo, F.F. Gao, F. Liu, S. Jin, Networked ISAC-based UAV tracking and handover toward low-altitude economy, *IEEE Trans. Wireless Commun.* **24**, 7670–7685 (2025)
- X. Zhang, K.H. Wang, X.B. Li, P. Liu, H. Shin, Joint task chain, power, and UAV trajectory optimization based on an integrated multi-UAV system, *IEEE Trans. Veh. Technol.* **74**, 12907–12920 (2025)
- A. Dagsan, E. Karasan, Resilient multi-hop autonomous UAV networks with extended lifetime for multi-target surveillance, *IEEE Trans. Netw. Serv. Manag.* **22**, 1500–1513 (2025)
- H. Li, G.L. Peng, X.B. Shan, M.Y. Zhao, W. Zhang, J.H. Wang, F. Cheng, Realizing high-speed target tracking by using multi-rate feedforward predictive control for the acquisition, tracking, and pointing system, *Defence Technol.* **49**, 137–151 (2025)

19. Z. Chen, W.X. Fu, R.T. Zhang, R.Y. Hong, W.B. Ye, Distributed collaborative target tracking of UAV formation considering passive detection efficiency, *Chin. J. Aeronaut.* **38**, 435–451 (2025)
20. L.H. Xiang, F.Y. Wang, W.J. Xu, T.K. Zhang, M. Pan, Z. Han, Dynamic UAV swarm collaboration for multi-targets tracking under malicious jamming: joint power, path and target association optimization, *IEEE Trans. Veh. Technol.* **73**, 5410–5425 (2024)
21. J.H. Yang, B. Wang, Z. Chang, Y.P. Zhao, Z.Y. Feng, F.Y. Hu, Joint trajectory planning and transmit resource optimization for multi-target tracking in multi-UAV-enabled MIMO radar system, *IEEE Trans. Intell. Transport. Syst.* **25**, 11422–11438 (2024)
22. A. Hazarika, M. Rahmati, Intelligent spatiotemporal freshness framework for multi-UAV target detection and tracking, *IEEE J. Miniatur. Air Space Syst.* **6**, 294–304 (2025)

Cite this article as: Jianwei Ren, Hua Wang, Hao Rong, Zexian Wei, Peixia Lv, Xiuqiong Li, Mou Bai, Radar-based interactive multi-model multi-target tracking algorithm for UAV swarms, *Int. J. Metrol. Qual. Eng.* **17**, 5 (2026), <https://doi.org/10.1051/ijmqe/2026002>